JASA ARTICLE

Influence of meteorological conditions and topography on the active space of mountain birds assessed by a wave-based sound propagation model

Arthur Guibard,[1,a)] Frédéric Sèbe,[2] Didier Dragna,[1] and Sébastien Ollivier[3]

[1]*Université Lyon, École Centrale de Lyon, INSA Lyon, Université Claude Bernard Lyon I, LMFA, CNRS UMR 5509, F-69134 Écully, France*

[2]*Université de Saint-Étienne, ENES/CRNL, CNRS UMR 5292, INSERM UMRS 1028, 42023 Saint-Étienne, France*

[3]*Université Lyon, Université Claude Bernard Lyon I, École Centrale de Lyon, INSA Lyon, LMFA, CNRS UMR 5509, F-69100 Villeurbanne, France*

ABSTRACT:

The active space is a central bioacoustic concept to understand communication networks and animal behavior. Propagation of biological acoustic signals has often been studied in homogeneous environments using an idealized circular active space representation, but few studies have assessed the variations of the active space due to environment heterogeneities and transmitter position. To study these variations for mountain birds like the rock ptarmigan, we developed a sound propagation model based on the parabolic equation method that accounts for the topography, the ground effects, and the meteorological conditions. The comparison of numerical simulations with measurements performed during an experimental campaign in the French Alps confirms the capacity of the model to accurately predict sound levels. We then use this model to show how mountain conditions affect surface and shape of active spaces, with topography being the most significant factor. Our data reveal that singing during display flights is a good strategy to adopt for a transmitter to expand its active space in such an environment. Overall, our study brings new perspectives to investigate the spatiotemporal dynamics of communication networks. © *2022 Author(s). All article content, except where otherwise noted, is licensed under a Creative Commons Attribution (CC BY) license (http://creativecommons.org/licenses/by/4.0/).* https://doi.org/10.1121/10.0011545

(Received 25 January 2022; revised 12 May 2022; accepted 13 May 2022; published online 3 June 2022)

[Editor: Mark A. Bee] Pages: 3703–3718

I. INTRODUCTION

In acoustic communication systems, the transmission of sound through the environment is a major source of signal degradation, caused by attenuation, absorption, and reflections. In bioacoustics and more particularly in the analysis of communication networks (Reichert *et al.*, 2021), one of the biggest challenges is the modeling of acoustic propagation to study the impact of the transmission channel on information exchange (Forrest, 1994).

Long-distance acoustic communication is used by many species of birds. Moreover, outdoor sound propagation is ruled by the influence of the habitat and environmental parameters (Dabelsteen *et al.*, 1993; Embleton, 1996). To study communication in birds, the bioacoustic notion of active space (AS) was introduced by Marten and Marler (1977) as being the "effective distance" of a signal, the distance from the source over which signal amplitude remains above the detection threshold of potential listeners. This definition was later extended to the "effective space" by McGregor and Dabelsteen, to describe communication networks (McGregor, 2005; McGregor and Dabelsteen, 1996). Considering an acoustic signal, the associated AS is determined by four factors: (1) amplitude of the signal at the source; (2) the rate at which signal energy attenuates by transmission through the environment; (3) amplitude of ambient noise in the environment; and (4) masked auditory threshold of receivers since the signal is embedded in a background noise (Brenowitz, 1982).

To the authors' knowledge, previous studies on long-distance acoustic communication have mostly considered homogeneous propagation environments and the maximum distance at which a transmitter could be heard as a criterion of AS. They were usually focused on the estimation of global excess attenuation (EA), signal-to-noise ratio (SNR), tail-to-signal ratio (TSR), or blur ratio (BR) over some frequency bands, depending on the distance to a transmitter, to estimate a radius of audibility. Many of these earlier works are based on field propagation experiments and playback experiments (Darden *et al.*, 2008; Lohr *et al.*, 2003; Loning *et al.*, 2022). The effect of transmitter and receiver heights on propagation has been investigated as well as environmental parameters (temperature, wind, humidity) (Dabelsteen *et al.*, 1993; Holland *et al.*, 1998; Jensen *et al.*, 2008; Mathevon *et al.*, 2005). The impact of diurnal

a)Also at: Université de Saint-Étienne, ENES/CRNL, CNRS UMR 5292, INSERM UMRS 1028, 42023, Saint-Étienne, France. Electronic mail: arthur.guibard@ec-lyon.fr

variations was investigated through a similar methodology (Dabelsteen and Mathevon, 2002; Henwood and Fabrick, 1979), as was the constraint of the rain on communication (Lengagne and Slater, 2002). Although these previous works provide answers about the effects of the environment on communication, they are not as suitable as a dedicated model could be.

Modeling acoustic propagation is crucial for studying animal communication, since recordings and playback experiments require a lot of time and material and can hardly be carried out on large areas. Therefore, propagation models have been proposed in the literature to estimate ASs of communication and information degradation. Most of them are based on simplified semi-empirical approaches as proposed by Henwood and Fabrick (1979) and Parris (2002) or more recently Raynor *et al.* (2017), in which the engineering-based SPreAD-GIS model was used. These models are computationally efficient, but they do not account for all the physics, and their outputs are often restricted to global indicators. Wave-based models, i.e., models that describe the wave propagation in time or in frequency domain, are more accurate, but due to their computational cost, they have been barely used in bioacoustics. A rare example is the study of Larom *et al.* (1997) that used a fast field program (FFP) model to show that the ASs of African savanna elephants depend on wind and temperature profiles.

Actually, topography and meteorological conditions depend on the habitat. These conditions obviously have a strong effect on AS, especially in mountainous areas, which represent a noticeably heterogeneous environment as stated by Reiners and Driese (2001). Moreover, it is essential to take these parameters into account to understand the impact of habitat on communication in both space and time. The study of these effects could provide interesting clues about the features of signal propagation in communication networks and their potential adaptation to the species' habitat (Mathevon *et al.*, 2008; Wiley and Richards, 1978).

To highlight the impact of the habitat on AS, we chose to work on an iconic species of high mountains: the rock ptarmigan (*Lagopus muta*). It is a species living in the northern hemisphere, in arctic or alpine habitat. Considering the period of intense vocal activity that is the breeding season in spring between April and June, environmental conditions and species behavior are known (Bossert, 1977; Watson, 1972). During this period, male ptarmigans sing at dawn to defend their territory and indicate their location. Their songs are often made during flights, which is the main territorial demonstration (Johnsgard, 2008; MacDonald, 1970).

At altitudes above 1800 m, alpine mountain ranges are usually still largely covered with snow. The propagation distance of this type of vocalization is about a few hundred meters. The vocalizing birds may be placed either on the ground or at a height of a several dozen meters. The characteristic frequencies of ptarmigan vocalizations are in the kilohertz range. These particularities imply a large-scale problem, which must be taken up by a computational method fast enough to be applicable.

The study of ASs is carried out using numerical simulations, allowing us to test a large number of propagation conditions. With this approach, we are trying to answer two questions: How do environmental constraints affect the vocal communication of mountain birds? And how do ptarmigans adapt and optimize their communication behavior?

The objectives of this study are (1) to develop a method to estimate ASs of a bird in heterogeneous environment; (2) to compare numerical results with *in situ* measurements to evaluate the model for the intended application; (3) to assess the influence of topography, temperature, and wind on the AS; and (4) to study the potential benefit of singing during display flight for the rock ptarmigan.

This article is organized as follows. Section II describes the model used in this study and the different assumptions made. The on-site measurement campaign and the comparisons between measurements and model estimations are detailed in Sec. III. Then Sec. IV presents an application of the previously tested model on a typical mountain site where a population of ptarmigan lives. Here, we investigate the variability of the AS in such a context. Concluding remarks are given in Sec. V.

II. ACTIVE SPACE AND PROPAGATION MODEL

A. Definition of the AS

Determination of AS is based on the propagation loss (PL), defined as the sound pressure level (SPL) relative to source level (SL). It represents the attenuation of the signal energy during propagation over an area. Following Brenowitz (1982), to set the PL threshold that defines the limits of the AS, several parameters must be considered: the source level (SL), the auditory threshold in masking noise, and the background noise.

ASs are investigated for the rock ptarmigan (*L. muta helvetica*), which is considered as a model of mountain bird. The rock ptarmigan uses acoustic vocalizations to communicate, especially during display flights, when it significantly increases its altitude up to 75 m from the ground (Johnsgard, 2008). Its vocalizations are sequences of pulse trains, with a pulse rate of 21 ± 3 ms and an energy distributed in the frequency range of 900–3700 Hz (Marin-Cudraz *et al.*, 2019), the maximum amplitude being around 1000 Hz. Neither the directivity nor the nearfield sound pressure level (SPL) (in dB relative to 20 μPa) of ptarmigan vocalizations is yet well characterized. For simplicity, in the present study, the directivity is assumed to be omnidirectional. To estimate the SPL, we assume that it is comparable to that of the corncrake (*Crex crex*), which is a non-passerine bird of similar size that also produces a broadcast call with pulsed signal. Its SL has been measured in the range of 80–101 dBSPL (Aubin and Mathevon, 2020; Ręk and Osiejuk, 2011). Therefore, the SL of rock ptarmigan vocalizations, defined as the SPL at 1 m from the source, is set at a median value of 90 dBSPL in the present study.

In this species, there is not much competition for vocal communication or selection pressure for encoding

https://doi.org/10.1121/10.0011545

information, because the density of birds is low with a relatively simple communication network (two to three neighbors maximum for each bird). In addition, they are the only birds that vocalize in a relatively low frequency range in this environment compared to other birds, and the latter are also scarce at this altitude. Thus, the situation is one of energetic masking due to background noise alone. For the purpose of this study, we arbitrarily set a detection threshold of 10 dB, regarded as the SNR required for comfortable communication in the sense of Dooling and Leek (2018). This value is sufficient to achieve the objectives of this article, but for a detailed study concerning the effect of ambient noise, it will be necessary to perform an estimation of the detection threshold of ptarmigan in noise. Background noise levels around 30 dBSPL or less were measured during clear daytime on the site considered in Sec. IV, where a population of ptarmigan lives. This value is kept throughout. From the last two elements, it is assumed that above a pressure level of 40 dBSPL, a receiver is able to detect and decode the information and is thus inside the AS. Below this 40 dBSPL threshold, the probability of detection decreases, and a receiver is no longer considered to be in the AS. In other words, considering a SL = 90 dBSPL and a detection threshold of 40 dBSPL, the AS is the area such that the propagation loss from the source does not exceed –50 dB. This PL threshold set to −50 dB could be corrected when the ptarmigan SL and detection threshold in noise are measured and could be different if considering other bird species.

B. Propagation model

In the context of atmospheric propagation, the choice of a model is a compromise between the computational cost, the complexity of environmental effects to be considered, and the type of results desired. For application to bird communication in mountains, the model must be able to compute vocalizations after propagation at long distances and high frequencies and include a stratified atmosphere with irregular topography.

The propagation model used here is based on the wide-angle parabolic equation (WAPE), described, e.g., by Salomons (2001), which is an efficient computational method for long-range sound propagation within the atmospheric boundary layer (ASL). It is obtained from the Helmholtz equation by considering forward propagating waves only. An $N\times$ 2D (two dimensions) approach is followed: the problem is not considered on a full three-dimensional (3D) geometry but on vertical slices, as illustrated in Fig. 1.

On each slice (x, z), the 2D axisymmetric WAPE is solved. The source is located at (x_s, z_s). Denoting by p_{PE} the pressure and introducing $q_{\mathrm{PE}} = \sqrt{R}\, p_{\mathrm{PE}}$, with $R = \sqrt{(x-x_s)^2 + (z-z_s)^2}$ the distance from the source, the WAPE equation can be written as

$$\left\{\frac{\partial}{\partial x} - \mathrm{i}k_0\mathcal{Q}\right\} q_{\mathrm{PE}}(x,z) = 0, \tag{1}$$

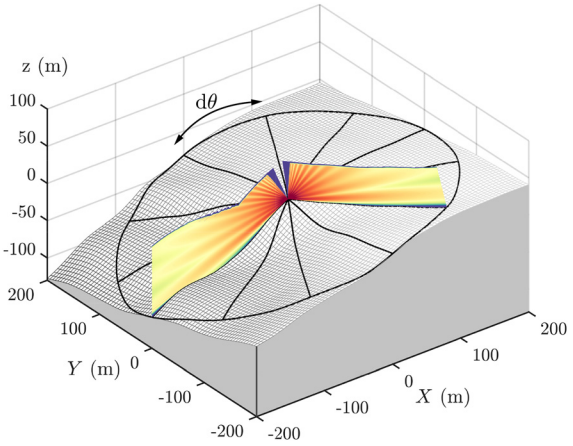

FIG. 1. (Color online) Principle of the $N \times$ 2D approach. Shown is PL on 2D domains.

where $k_0 = \omega/c_0$ is the reference wave number, c_0 is the reference sound speed chosen at the ground level, and $\omega = 2\pi f$, with f the frequency. The pseudo-differential operator $\mathcal{Q}$ is written as a Padé (1,1) approximation,

$$\mathcal{Q} = \frac{1+\eta_1\mathcal{L}}{1+\eta_2\mathcal{L}}, \tag{2}$$

with $\eta_1 = 3/4$ and $\eta_2 = 1/4$. The operator $\mathcal{L}$ is given by

$$\mathcal{L} = \epsilon_{\mathrm{eff}} + \frac{1}{k_0^2}\frac{\partial^2}{\partial_z^2}, \tag{3}$$

with $\epsilon_{\mathrm{eff}} = c_0^2/c_{\mathrm{eff}}^2 - 1$. The parameter c_{eff} is the effective sound speed, which accounts for temperature and wind variations. Its calculation is detailed in Sec. III A 2. The effective sound speed approach is a reasonable approximation in the lower ASL for low wind speed. Note that Ostashev *et al.* (2020) recently proposed a parabolic equation (PE) formulation that improves the inclusion of wind profiles. In addition, full 3D PE formulations (Khodr *et al.*, 2020) have been already proposed in the literature for atmospheric sound propagation. Although they describe 3D propagation effects, they induce a large increase in the computational cost. For application to bioacoustics, a 2D approach was deemed to be sufficient.

The topography is described by a succession of flat domains of fixed length, defined by an angle a with respect to the horizontal x axis, as suggested by Blairon *et al.* (2002) and Lihoreau *et al.* (2006). In each domain, the (x_n, z_n) coordinate system is rotated to keep the x_n axis parallel to the ground, as shown in Fig. 2. The length of each domain is set to 5 m, which is sufficient to properly fit most real topographies. For the first domain, the calculation is initialized by the wide-angle starter, which accounts for the source image weighted with a complex reflection coefficient, derived in Salomons (2001). This reproduces a monochromatic omnidirectional point source in the acoustic far field ($k_0R \gg 1$). Note that the propagation model does not allow a precise prediction of the near field. The amplitude of the source is set so

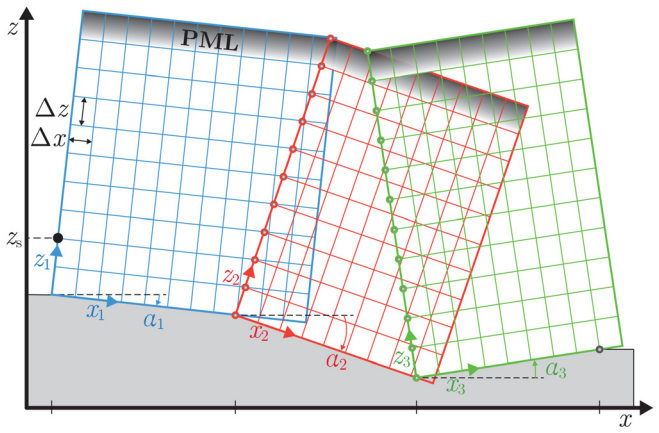

FIG. 2. (Color online) Sketch of rotated PE method: grids in the (x_n, z_n) planes, with fixed tangent grid spacing Δx and orthogonal grid spacing Δz. A PML is set at the top of each domain to ensure a reflectionless condition.

that the SPL in free field at 1 m is equal to SL. For the other domains, the starter is obtained by interpolating the pressure field of the previous domains.

In each domain, the problem is discretized using the Crank–Nicholson marching scheme in the propagating direction x_n and second-order finite-differences in the transverse direction z_n. The discretization steps are fixed to $\Delta x = \Delta z = \lambda/10$, with the wavelength $\lambda = c_0/f$. The WAPE method ensures accurate results within a propagation angle of 40° above and below the x direction (Ostashev *et al.*, 1997). This implies that the angle between two consecutive domains must remain between these limits.

At the top of each domain, a perfectly matched layer (PML), based on the work of Collino (1997), is implemented as a non-reflecting boundary condition. At the ground, a surface admittance boundary condition is applied. This assumes that the ground is locally reacting. Because of its small flow resistivity, snow is, however, usually considered as an extended-reacting ground. To mimic the effect of extended reaction at long distance, the normalized surface admittance β_s is evaluated from that of an extended-reacting hard-backed porous layer of constant effective thickness e (Li *et al.*, 1998) at grazing incidence (angle of incidence equal to $\pi/2$). This yields

$$\beta_s = \beta_c \frac{\sqrt{n^2-1}}{n} \tanh\left(-\mathrm{i}k_0 e\sqrt{n^2-1}\right), \tag{4}$$

with $n = k_c/k_0$ and β_c and k_c the characteristic admittance and the wavenumber of the snow layer. The acoustic properties of the snow (β_c, k_c) are defined according to the phenomenological model proposed by Bérengier *et al.* (1997),

$$\beta_c = \frac{\Omega}{q}\left[1-\frac{\omega_1}{\mathrm{i}\omega}\right]^{-1/2}\left[1-\frac{\omega_2}{\mathrm{i}\omega}\right]^{-1/2}\left[1-\frac{\omega_3}{\mathrm{i}\omega}\right]^{1/2}, \tag{5}$$

$$k_c = k_0 q\left[1-\frac{\omega_1}{\mathrm{i}\omega}\right]^{1/2}\left[1-\frac{\omega_2}{\mathrm{i}\omega}\right]^{-1/2}\left[1-\frac{\omega_3}{\mathrm{i}\omega}\right]^{1/2}, \tag{6}$$

with $\omega_1 = R_s\Omega/(\rho_0 q^2)$, $\omega_2 = R_s/(\rho_0 \mathrm{Pr})$, $\omega_3 = \gamma R_s/(\rho_0 \mathrm{Pr})$, ρ_0 the air density at the ground, $\gamma = 1.4$ the specific heat ratio, and $\mathrm{Pr} = 0.7$ the Prandtl number. This model uses three parameters: the airflow resistivity of the porous structure R_s, the porosity of air-filled connected pores Ω, and the tortuosity q^2. Note that other impedance models can also be used, such as the relaxation model (Wilson, 1993) or the slit-pore model (Attenborough and van Renterghem, 2021).

The PE method is a frequency-domain approach. For broadband signals, the calculation must be repeated for all frequencies of interest. In addition, it can be noted that the time signal after propagation can be determined from a broadband spectrum using an inverse Fourier transform. Several remarks can be made with regard to the limits of application of this model in mountainous areas. First, backscattering is neglected, and thereby the possible echoes are not considered. Second, three-dimensional effects relative to wind and topography are neglected by the $N\times$ 2D approach.

C. 3D pressure calculation and AS

The determination of the AS from the PE solution is detailed. Since the PE solution does not account for atmospheric absorption, a correction is then applied to the pressure,

$$p(f,x,z) = p_{\mathrm{PE}}(f,x,z)\,\exp\left[-\alpha(f)R(x,z)\right], \tag{7}$$

where the atmospheric absorption factor α is based on the ISO 9613–1 standard (ISO, 1993). From this, the SPL $L_p(x,z)$ is calculated with

$$L_p(x,z) = 10\log_{10}\left(\frac{|p(x,z)|^2}{p_{\mathrm{ref}}^2}\right), \tag{8}$$

with $p_{\mathrm{ref}} = 2\times10^{-5}$ Pa. Finally, the propagation loss is determined in each slice with $\mathrm{PL}(x,z) = L_p(x,z) - \mathrm{SL}$.

To obtain the acoustic field on the whole 3D geometry, PE calculations are repeated for each vertical slice by varying the angle θ around the z axis, with a step $\mathrm{d}\theta$, as shown in Fig. 1. The 2D topography profiles are obtained by interpolation of the 3D topography. We further consider an angular step of $\mathrm{d}\theta = 2°$. A map of PLs around the source at a given height above the ground, chosen as 1 m, is deduced as illustrated in Fig. 3.

The area of the AS, denoted by A, is then computed from the PL map. For that, the PL is determined at receivers placed at 1 m height from the ground, with a step $\mathrm{d}x = 1$ m. The receivers for which the propagation loss is above the threshold are identified. The AS area is thus the sum of elementary surface areas $x\,\mathrm{d}x\,\mathrm{d}\theta$. Because of the limitation in the propagation angle associated with the PE method, receivers placed under this angle near the source are not considered in the PE calculation and are assumed to belong to the AS.

https://doi.org/10.1121/10.0011545

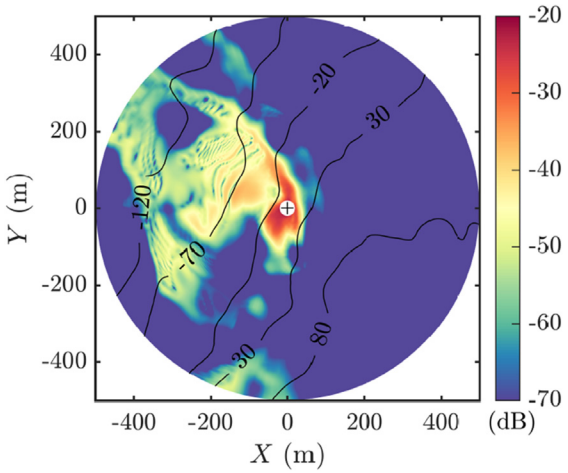

FIG. 3. (Color online) Map of the PL at 1 m height, for a frequency of 1000 Hz. Contour lines are drawn every 50 m in thin lines. Conditions: topography 1 in Fig. 13, homogeneous atmosphere, and $z_s = 1$ m.

III. COMPARISON OF WAPE MODEL WITH ON-SITE MEASUREMENTS

To validate the prediction capacity of the model, measurements were performed in a mountain environment. This section details how the environmental parameters were measured and presents the comparisons between the results of the acoustical field measurements and the corresponding numerical simulations.

A. Experiments

1. Measurement site

The measurements were conducted in October 2020 in the French Alps on the site of Col du Lac Blanc in the Massif des Grandes Rousses [45.13 N, 6.11 E, 2720 m above sea level (a.s.l.)]. This site was chosen because two research institutes [Centre d'Etudes de la Neige (CEN) and the Institut National de Recherche pour l'Agriculture, l'Alimentation et l'Environnement (INRAE)] maintain two complementary automated weather stations (AWSs) at this location. This allows us to obtain the meteorological data during the experiments. Despite the site not being dedicated to the monitoring of rock ptarmigan population, it is typical of mountain environments where the rock ptarmigan lives.

The site is a mountain pass that presents a hill shape of 15 m height in its longitudinal section (north-south direction), called hereafter the "hill." The wind is naturally channeled in this north-south direction. The weather instrumentation is installed at the top of the small hill. A digital elevation model (DEM) of the site with bare ground was determined by Guyomarc'h *et al.* (2019), using a laser scanning technique (Fig. 4). The DEM has a horizontal resolution of 1 m and a vertical resolution of 0.1 m. The chosen propagation zone is such that echoes are absent or manageable in post-processing thanks to the short duration of the source signal.

Three transects, depicted in Fig. 4, were chosen on either side of the mountain pass. Transects t1 and t2 are

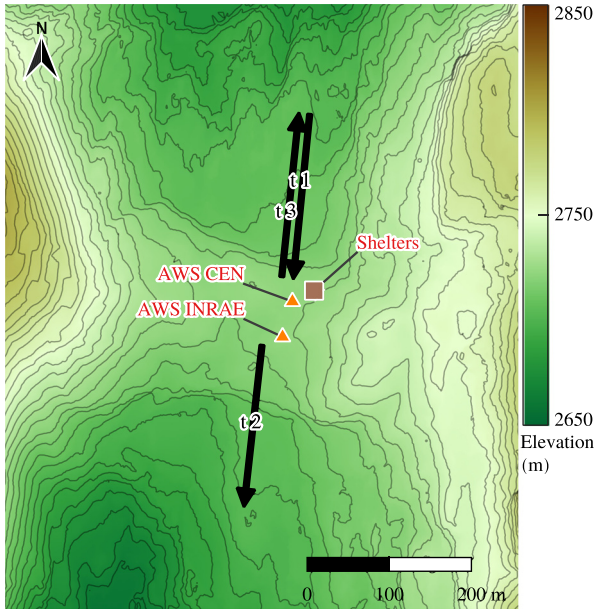

FIG. 4. (Color online) Map of the measurement field at Col du Lac Blanc (Massif des Grandes Rousses, France), with 5 m contour lines. Propagation transects (t1, t2, t3) and their direction are drawn with black arrows. AWSs (AWS CEN) and (AWS INRAE) are depicted by triangles.

directed to the south, uphill and downhill, respectively. Transect t3 is reversed with respect to t1 and thus faces north downhill. Several measurements were carried out on these different transects in various weather conditions. Among the available data, results for four representative configurations, denoted by A, B, C, and D, are presented in this paper and summarized in Table I. The configurations A and B are for similar meteorological conditions but for two different topographies, transects t1 and t2. The configurations C and D are both for the same topography, transect t3, but with different meteorological conditions.

2. Meteorological data

Atmospheric conditions during the propagation experiments were available from two AWSs, named "AWS CEN" and "AWS INRAE," which are located close to the acoustic source (Figs. 5 and 6). Temperature and humidity were measured by five sensors (HMP155A, Vaisala, Vantaa, Finland) mounted on the AWS CEN at heights of 0.8, 1.3, 3.2, 5, and 7 m above the snow surface. Wind direction and velocity were obtained from the AWS INRAE. The wind vane (W200P-01,

TABLE I. Detailed measurement configurations (A, B, C, D) with the transect concerned (t1, t2, t3), the propagation condition, and the gradient of effective sound speed near the ground Δc_{eff} ($\text{m}\cdot\text{s}^{-1}$).

Configuration	Transect	Condition	Δc_{eff} ($\text{m}\cdot\text{s}^{-1}$)
A	t1	Strong downward	4.3
B	t2	Strong downward	6.4
C	t3	Slight upward	−0.3
D	t3	Moderate upward	−1.8

Vector Instruments, Saint Asaph, UK) was mounted at a height of 11.08 m, and five anemometers (Vector Instruments A100LK) were mounted at heights of 1.76, 3.25, 4.1, 7.25, and 9.42 m. Data discussed in the following paragraphs are the average temperature and the average and standard deviation of the wind velocity, both integrated over periods of 10 min and measured during the sound propagation experiments.

The raw data of temperature and wind speed measured with the two AWSs are plotted with markers in Fig. 7 as functions of the height above the snow cover z_g. The wind speed profile presents a significant acceleration in the first 4 m above the ground. This is due to a localized Venturi effect induced by the hill in the middle of the pass.

Meteorological data were extrapolated by means of an iterative fitting procedure based on the Monin and Obukhov (1954) similarity theory (MOST). One of the assumptions of MOST is that the ground is flat and homogeneous, which is clearly not the case here. However, with no better description of the atmosphere, MOST is used as it provides representative wind and temperature profiles encountered in the ASL. Wind and temperature profiles are given by

$$U_{\mathrm{fit}}(z_g) = \frac{u_*}{\kappa}\left[\ln\left(\frac{z_g + z_0}{z_0}\right) - \psi_w\left(\frac{z_g}{L_{\mathrm{MO}}}\right)\right], \tag{9}$$

$$T_{\mathrm{fit}}(z_g) = T_0 + \frac{\theta_*}{\kappa}\left[\ln\left(\frac{z_g + z_0}{z_0}\right) - \psi_t\left(\frac{z_g}{L_{\mathrm{MO}}}\right)\right] + \alpha_0 z_g, \tag{10}$$

with $\kappa = 0.41$ the von Kármán constant, u_* the friction velocity, T_0 the air temperature near the ground, θ_* the temperature scale, L_{MO} the Monin–Obukhov length, $\alpha_0 = -0.01$ K·m^{-1} the dry adiabatic lapse rate, and z_0 the roughness length of the ground surface set to 0.01 m. The functions ψ_w and ψ_t are derived from the Businger–Dyer relations, as detailed in Salomons (2001). To get rid of the local acceleration discussed above, the fitting procedure takes into account the five measured temperature values but only the three wind speeds at the upper positions. The fitted profiles are plotted in Fig. 7 according to the four configurations. The fit with the measurements appears appropriate for the temperature $T(z_g)$. For the wind speed $U(z_g)$, noticeable discrepancies are observed: they are related to the local acceleration near the ground. The corresponding MOST parameters obtained are listed in Table II.

Typical values for u_* are indicated in Ostashev and Wilson (2016): 0.1, 0.3, and 0.6 m/s correspond to a light, moderate, and strong wind condition, respectively. Therefore, all four configurations are under light or moderate wind conditions as u_* is between 0.13 and 0.19 m/s. The angle ψ between measured wind direction and each transect remains relatively constant during each measurement period as shown by the values of its standard deviation σ_ψ, given in Table II.

The extrapolated profiles of wind speed and temperature are used to determine the effective sound speed. It is defined as the sum of the sound speed and the horizontal component of the wind speed in the direction of propagation,

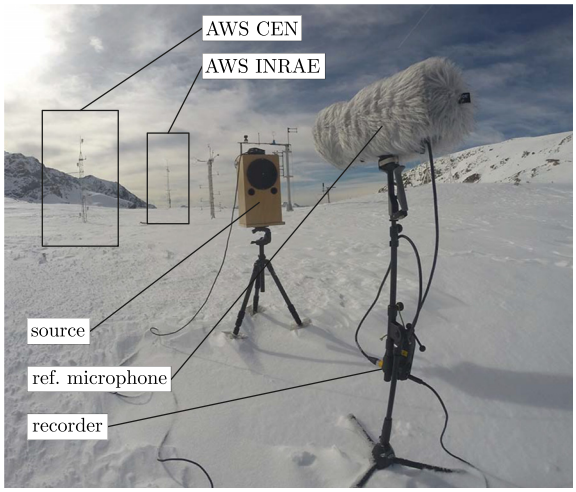

FIG. 5. (Color online) Picture of the measurement setup for acoustic propagation: source, reference microphone, and two AWSs: AWS CEN and AWS INRAE (setup of transect 3).

$$c_{\mathrm{eff}}(z_g) = \sqrt{\gamma r_{\mathrm{air}} T_{\mathrm{fit}}(z_g)} + U_{\mathrm{fit}}(z_g)\cos\psi, \tag{11}$$

with ψ the angle between the mean wind direction and the transect direction from the source and $r_{\mathrm{air}} = 287\,\mathrm{J}\cdot\mathrm{kg}^{-1}\cdot\mathrm{K}^{-1}$ the specific gas constant for dry air. The effective sound speed profiles are plotted in Fig. 7. It appears that configurations A and B present a predominant effect of the temperature gradient, while configurations D show a predominant effect of the wind speed gradient. Finally, configuration C is a nearly homogeneous case.

To characterize the sound speed gradient near the ground, the parameter $\Delta c_{\mathrm{eff}} = c_{\mathrm{eff}}(z_g = 20\,\mathrm{m}) - c_0$ is introduced. It determines the atmospheric refraction: upward for $\Delta c_{\mathrm{eff}} < 0$, downward for $\Delta c_{\mathrm{eff}} > 0$, or homogeneous for $\Delta c_{\mathrm{eff}} \approx 0$. Downward condition is induced by a temperature inversion and/or a downwind condition. It leads to refraction of sound waves toward the ground and to an increase in sound level at the vicinity of the ground. Conversely, upward conditions occur for negative temperature gradients and/or for headwind. Now sound waves are refracted toward the sky, inducing shadow zones at long range. The values of Δc_{eff} for the four configurations are given in Table I: A and B correspond to strong downward refracting conditions, and C and D correspond to slight and moderate upward refracting conditions, respectively.

TABLE II. Parameters of the fitted temperature and wind profiles for configurations (A, B, C, D): Monin–Obukhov length L_{MO}, air temperature near the ground T_0, temperature scale θ_*, friction velocity u_*, angle between wind direction and the transect $\psi \pm \sigma_\psi$ (σ as the standard deviation), and RH.

Configuration	L_{MO} (m)	T_0 (°C)	θ_* (K)	u_* (m·s^{-1})	$\psi \pm \sigma_\psi$ (deg)	RH (%)
A	8.4	−6.57	0.09	0.10	22 ± 12	98
B	6.4	−4.04	0.13	0.11	6 ± 13	40
C	9	−0.76	0.01	0.03	314 ± 30	90
D	205	−1.06	0.00	0.09	20 ± 19	96

https://doi.org/10.1121/10.0011545

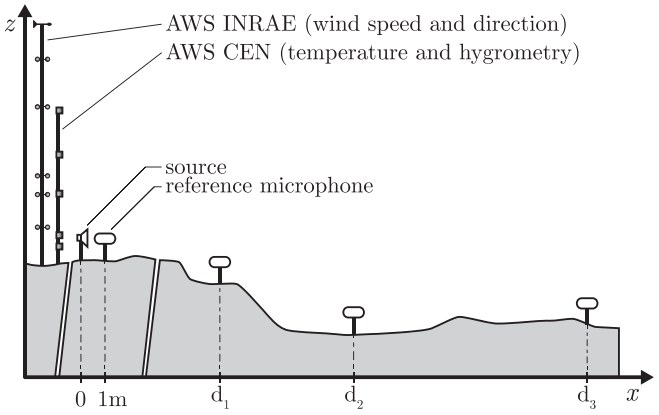

FIG. 6. Sketch of the measurement setup on a transect. Source–microphone distances are $d_1 = 50$ m, $d_2 = 100$ m, and $d_3 = 200$ m.

In addition to average meteorological profiles, two other conditions are defined considering each configuration to investigate the influence of meteorological variability on sound propagation. For that, it is assumed that the temperature evolves more slowly with time than the wind speed and, as a consequence, that the meteorological variability is only due to that of the wind speed. Two other sets of temperature and wind speed profiles are thus obtained using MOST from $T(z)$ and from the reduced values $U(z) - 2\sigma_U(z)$ and increased values $U(z) + 2\sigma_U(z)$, where $\sigma_U(z)$ is the standard deviation of the wind speed given by the AWS. They are then used to determine the corresponding effective sound speed profiles.

Finally, the relative humidity (RH) (Table II), used to calculate the atmospheric absorption factor α, is determined as the time average of the values measured by the five humidity sensors.

3. Acoustic propagation measurements

The sound source was a high power portable loudspeaker, designed and built for the experiment. Its directivity was measured in an anechoic chamber. Microphones used were four Beyerdynamic (Heilbronn, Germany) MM1 audio microphones covered with a RØDE (Sydney, Australia) Blimp MkII windscreen (Fig. 5). Four H6 audio recorders (Zoom, San Jose, CA) were used. The source and the microphones were placed at 1 m above the snow cover surface. A reference microphone was first calibrated at 94 dBSPL at the frequency of 1000 Hz with a class 1 calibrator (CR517, Cirrus, Hunmanby, UK). A relative calibration of the microphone with their recorder was performed at the same time for all microphones in front of the source with a 50 dBSPL, 1000 Hz signal. This procedure allowed us to synchronize the recordings. The reference microphone was then positioned at 1 m from the loudspeaker as seen in Fig. 6, and the three other microphones were moved 50, 100, and 200 m away from the source using a GPS receiver. The relative distances were measured using a laser telemeter with an accuracy on the order of ± 1 m.

The source signal was a 1 s chirp made of a sinus sweep with frequency increasing exponentially from 100 to 3600 Hz. To ensure that the level measured at 200 m from the source is significantly higher than the background noise, the SL is set to 110 dBSPL at 1 m from the loudspeaker, which is higher than the estimated level of the vocalizations of the ptarmigan. This allows for relevant comparisons with our model in the following. The chirp was repeated every 10 s during 10 min. This led to a series of 60 measured waveforms per 10 min period that can be related to corresponding meteorological data since the weather stations provide the mean wind and temperature profiles averaged over 10 min periods.

The background noise SPL was always at least 10 dB lower than the levels measured at the microphones over the frequency band 300–3000 Hz. It is therefore reasonable to consider that the background noise had no influence on the measured pressure levels.

4. Snow impedance

Several techniques can be used to measure ground impedance (Albert, 2001; ANSI/ASA, 2010; Datt *et al.*, 2016; Guillaume *et al.*, 2015; Moore *et al.*, 1991; Nordtest, 1999). In the present study, the snow impedance was measured *in situ* using the method proposed by Guillaume *et al.* (2015), which is suited for grazing angles and has been

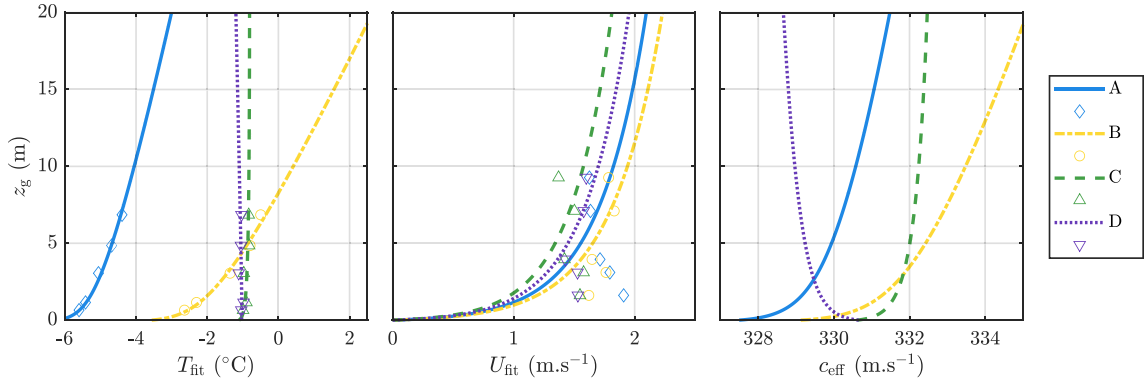

FIG. 7. (Color online) Fitted temperature T_{fit} and wind U_{fit} profiles and deduced effective sound speed profile c_{eff} from the four measurements carried out (A, B, C, D) are depicted by lines. Corresponding measured data $U(z_g)$, $T(z_g)$ are depicted by markers.

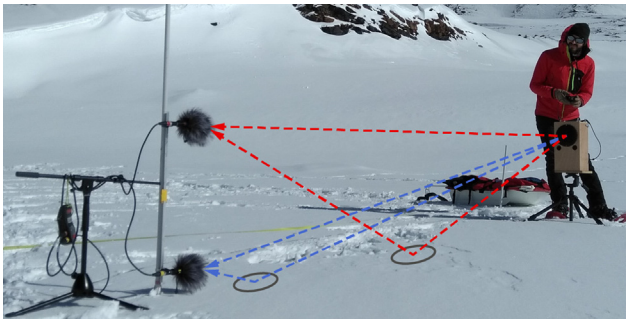

FIG. 8. (Color online) Picture of the measurement setup for snow impedance. The different wave paths are represented by dotted lines. The loudspeaker is on the right, and two microphones are on the left.

shown to provide reliable data for long-range propagation computation (Dragna *et al.*, 2014). These measurements were made just before or after the propagation experiments, at a single location representative of the snow cover along the propagation path. The method consists in carrying out a propagation experiment between a source placed at 0.7 m from the ground and two microphones 4 m apart and placed at 0.1 and 0.7 m from the ground, as shown in Fig. 8. The source signal was a 1 s exponential frequency chirp from 100 to 3000 Hz, repeated 50 times at 4 s intervals. From the measured signals, the transfer function between the two microphones is calculated and then compared to the analytical transfer function, whose impedance parameters are adjusted to adapt to the measured data. Assuming that the ground is flat and the snow cover is uniform with a constant thickness, the transfer function can be calculated analytically using the Weyl–Van der Pol equation [see, e.g., Attenborough and van Renterghem (2021)]. Note that extended reaction has been taken into account in the analytical formulation. The four parameters of the surface admittance model [see Eqs. (4)–(6)] are then manually fitted to match the analytical transfer function with the measured one. The corresponding analytical and measured transfer functions are represented in Fig. 9 for the 2 days concerned. Table III indicates the resulting parameters of the impedance model. These results are consistent with those in Moore

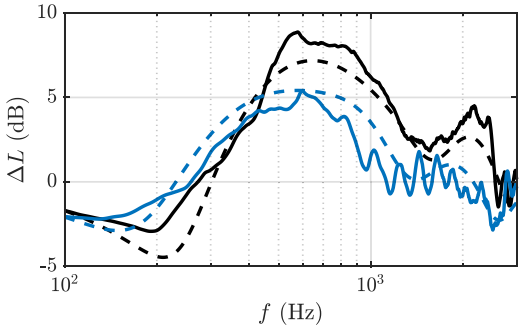

FIG. 9. (Color online) Transfer function for the determination of snow impedance ΔL for configurations A and B (black lines) and configurations C and D (blue lines): measure (solid lines) and analytical fit (dashed lines).

TABLE III. Impedance parameters obtained during the 2 days of measurement on the site of Lac du Col Blanc: the effective thickness e, the airflow resistivity R_s, the porosity Ω, and the tortuosity q^2. The corresponding configurations (A, B, C, D) are indicated.

Configuration	e (m)	R_s (Pa · s · m^{-2})	Ω	q^2
A, B	0.13	10 000	0.6	1.3
C, D	0.2	7000	0.6	1.3

et al. (1991), Albert (2001), and Datt *et al.* (2016) for the same type of snow (powder snow).

It should be noted that the method is based on assumptions that are not always valid for this type of *in situ* measurement of snow impedance. First, in the model, the snow depth is assumed to be constant, while in reality, it is not uniform over the entire propagation domain. However, specific tests carried out during the present measurement campaign in different parts of the domain showed that the surface impedance in the frequency band of interest was only slightly modified by the thickness of the snow layer, as soon as it exceeds 15 cm. This thickness value is comparable to the computed values of the effective thickness e. Second, the ground is assumed to be flat. This assumption is reasonable for the measurements presented here because the layer of fresh snow present on the site had a homogeneous structure and a smooth surface, but this may not always be the case, especially when the wind generates a wavy surface and when the surface layer is made of frozen wet snow. This could induce a rough surface, which is outside the scope of this method.

B. Comparisons with the propagation model

1. Description

To fairly compare the results of the propagation model to the measurements, the measured data were processed as explained in Sec. III A 2 for the meteorological conditions and Sec. III A 4 for the snow impedance to obtain input data of the numerical simulations. The four configurations (A, B, C, D) are described in Table I, with corresponding MOST parameters in Table II and snow impedance parameters in Table III. The position of each transect is shown in Fig. 4, and their corresponding topographic profiles are shown in Fig. 10. As the DEM of the site is given for a bare ground, it does not account for the snow cover. The DEM is then corrected by adding a snow cover estimated at 20 cm on the entire site, based on our observations.

In addition, a significant snow accumulation was noticed along the slopes of the hill: the snow cover was measured using a probe in the middle of the slopes, yielding a depth of 1 m on the north slope and of 1.4 m on the south slope. An additional correction is thus applied to the DEM along the hill slopes to account for this accumulation.

With this corrected DEM, the microphones at $x = 100$ m for configuration B and at $x = 50$ m for configurations C and D are in geometrical shadow zones, where the source has no

https://doi.org/10.1121/10.0011545

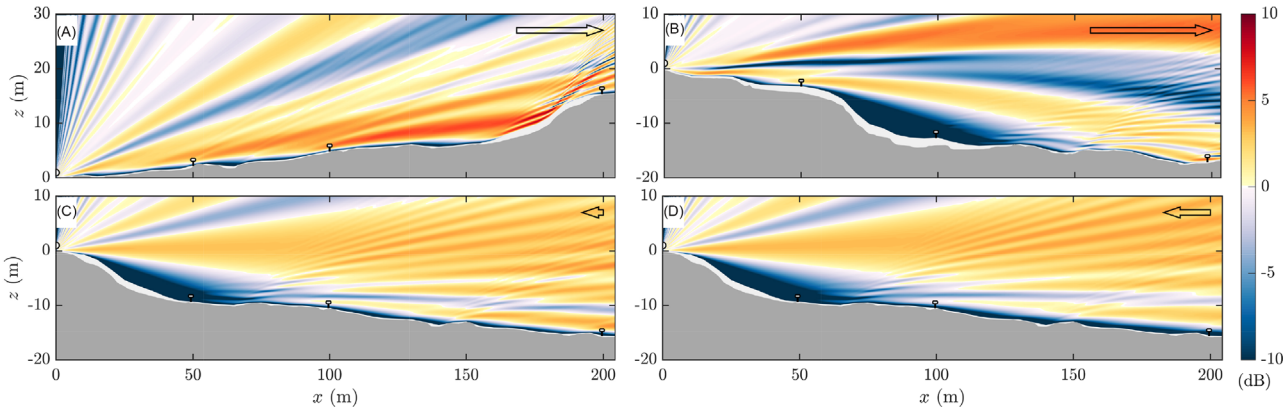

FIG. 10. (Color online) Pressure levels relative to free field ΔL simulated at 1000 Hz, for four configurations (A, B, C, D): actual terrain profile relative to source position $x_S = 0$, $z_S = 1$ m (gray surface); snow cover depth considered over the bare ground and smoothed every 5 m (white surface); microphone positions $x = 50$, 100, and 200 m (dots); and arrows of length proportional to Δc_{eff}. Scale $z/x = 1/2$.

direct view of the receivers assuming a homogeneous atmosphere with no refraction effect. Low SPLs are expected in these areas.

Computations are performed for the effective sound speed profile obtained from the average wind speed and temperature (T, U) reported in Sec. III A 2 as well as for the profiles accounting for wind speed variability (T, $U \pm 2\sigma_U$).

2. Results

The 2D maps of the SPL relative to the free-field solution $\Delta L = \text{PL} + 20\log_{10}(R)$ computed for $f = 1000$ Hz are plotted in Fig. 10 for the four configurations. The quantity ΔL represents the deviation from SPL in free field due to atmospheric refraction and diffraction effects. The 2D maps show a strong decrease in the acoustic pressure at the vicinity of the ground caused by the snow cover. The pressure level is equivalent to or lower than that in free field in the first centimeters above the ground. In all four cases, ΔL has a variability of ± 10 dB for the majority of microphone positions except in the shadow zones. Shadow zones are noticed at $x = 100$ m for configuration B and at $x = 50$ m for configurations C and D. They are visible in Fig. 10, where ΔL approaches –10 dB or less (in dark blue).

The influence of the sound speed gradient Δc_{eff} is visible on the distribution of the acoustic field across the domain. In particular, in case B, the acoustic energy is directed to the ground beyond 150 m due to downward conditions. This refraction reduces the size of the shadow zone compared to the homogeneous case. Conversely, case D shows an upward refraction due to upwind condition.

The results of the simulations are compared to the measurements using the relative SPL ΔL_p defined as $\Delta L_p(x,z) = L_p(x,z) - L_p(x_{\text{ref}}, z_{\text{ref}})$, with the reference point located at 1 m in front of the source. The pressure obtained with the WAPE method is not accurate in the nearfield. Then the reference level $L_p(x_{\text{ref}}, z_{\text{ref}})$ is obtained from the analytical solution of the Weyl–Van der Pol equation over a flat ground of the same impedance (Attenborough and van Renterghem, 2021). To match experimental conditions, the reflected wave amplitude is corrected by the source directivity of the loudspeaker.

For each configuration, the frequency spectrum at the receivers is deduced from computations carried out on 200 frequencies logarithmically distributed over the 200–3000 Hz band. The relative pressure levels ΔL_p obtained at each receiver ($x = 50, 100, 200$ m) are plotted in Fig. 11, along with the 60 measured spectra. In this figure, we can see for all configurations that the SPL computed by the propagation model closely matches the measurements both in downward and upward condition over the frequency band 200–3000 Hz, except for some pronounced interferences. Moreover, the variability in the frequency of the destructive interference pattern is fairly well reproduced by taking into account the variability of the wind speed. The discrepancy on the absolute position of the interference patterns can be explained by the piecewise linear approximation of the topography used in the propagation model, by the uncertainty on the wind speed along the propagation path, and by the uncertainty on the position of microphones. Note that small uncertainties influence the spectra calculated by the model and in particular above a certain frequency whose wavelength approaches the size of the error on the geometry. This could also be due to the single value approximation of the snow impedance boundary condition. The level estimations in shadow zone for configuration B at 100 m show a relative agreement in variability due to wind speed. For configurations C and D in upward conditions, the measured pressure levels are also in good agreement with the propagation model in the geometrical shadow zone of transect 3 at 50 m and in the shadow zone at 200 m induced by upward refraction.

An additional comparison between measurements and numerical results is shown in Fig. 12. It presents the boxplots of ΔL_p integrated on the 1000 Hz octave band for the 60 measured waveforms at the three microphones and for the four cases. The 1 kHz octave band is chosen because the amplitude of ptarmigan vocalization is maximal in this band. For readability, the boxplots are centered on the median of the measured data. The four configurations are sorted according to the sound speed gradient Δc_{eff}.

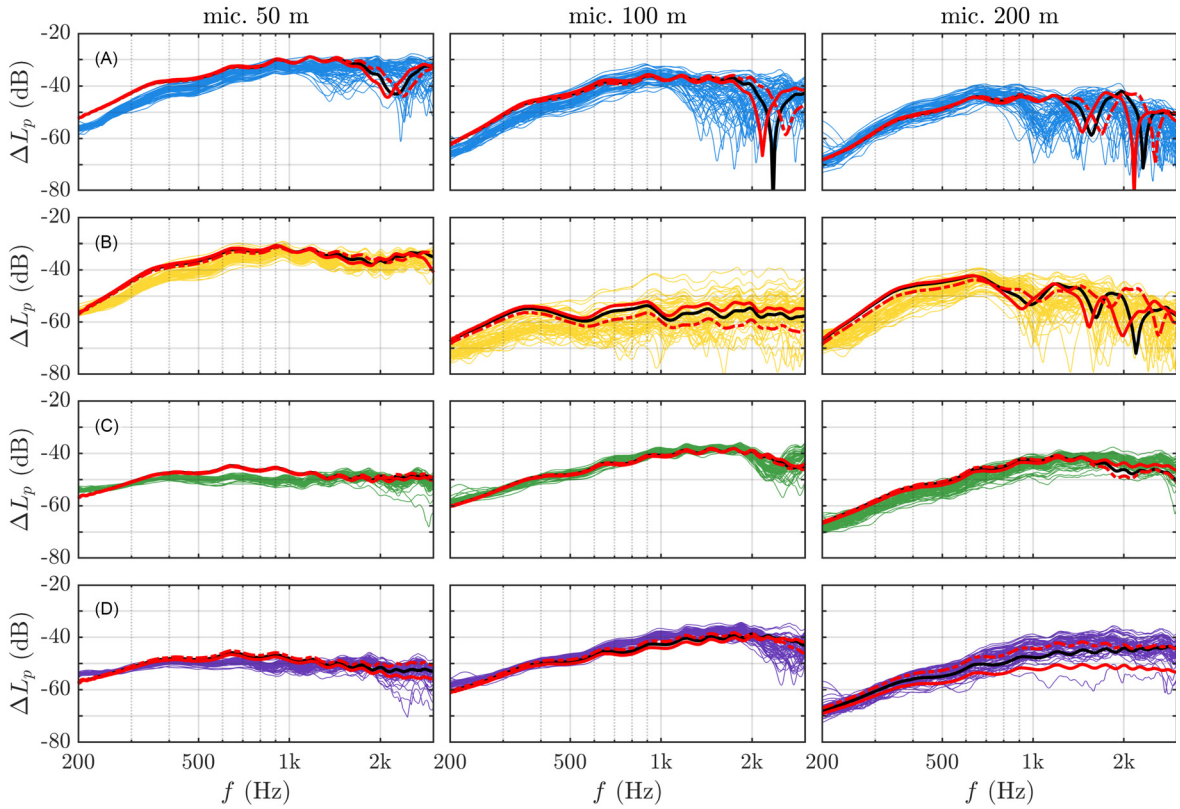

FIG. 11. (Color online) ΔL_p determined from the measurements (in thin color line) and simulated for c_{eff} deduced from (T, U) in black solid line, (T, $U-2\sigma_U$) in red dashed line, and (T, $U+2\sigma_U$) in red solid line. These results are for the four cases (A, B, C, D from top to bottom) and for the three microphone locations ($x=50$, 100, and 200 m from left to right). Same colors as in Fig. 6.

The boxplots indicate the variability of the measured SPL. The SPL calculated with the propagation model for the profiles of average temperature and wind speed (T, U) and for the profiles accounting for wind speed variability (T, $U\pm2\sigma_U$) are also plotted in Fig. 12.

The correspondence between the median of the measured SPL and the SPL predicted with the propagation model for the average meteorological conditions is first analyzed. For all conditions, the model provides an accurate estimation of the levels measured in the 1000 Hz band for receivers placed at 50, 100, and 200 m. The differences are between –3.1 and +2.9 dB, including estimate levels in geometrical shadow zones (case B at 100 m and C and at 50 m) and also in refraction-induced shadow zone (case D at 200 m). At a distance of 50 m, meteorological effects have little influence, and overestimates are more likely due to topography approximation and uncertainty in snowpack depth, which define the line of sight and therefore the geometric shadow areas. The propagation model also allows analysis of the variability of the SPL due to sound speed profiles. For that, the dispersion between the first and third quartiles in the boxplots is compared with the difference in the SPL calculated for the profiles (T, $U-2\sigma_U$) and (T, $U+2\sigma_U$). A fair agreement is obtained overall. However, in case A, the simulated variability is not accurately reproduced at 50 and 100 m. This is due to inaccurate prediction of the destructive interference frequency on the 1000 Hz octave band. In case B, the level variability matches well the measurements, except at 50 m. Cases C and D also show a good agreement for the three microphone positions. This implies in particular that the variability of the measured SPL is partly explained by the variability of the wind speed. However, we only consider the variability of wind speed at the weather station, while pressure levels may depend on local wind speed and direction fluctuations along the propagation path as well as local changes in the temperature profile.

In summary, these results show that predictions of SPLs using a wave propagation model are consistent with field measurement. Levels are correctly estimated in shadow zones, whether geometric or headwind induced, allowing the model to be used to study the AS of birds in a mountainous habitat. However, we note that partial knowledge of input parameters and approximations may induce errors in the prediction of levels. We mentioned that the approximation of terrain profiles and snowpack thickness can shift the location of geometric shadow zones. Atmospheric parameters can hardly be characterized over the entire area of interest and must be extrapolated from weather stations. In addition, the model does not account for rapid temporal or spatial variations in wind direction or for turbulence. The impedance value determined for one location was applied to the entire propagation path because the snow parameters in the chosen measurement site were nearly constant. However, in more

https://doi.org/10.1121/10.0011545

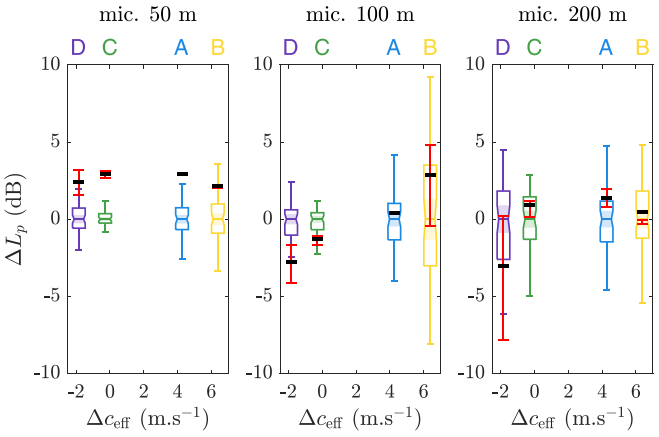

FIG. 12. (Color online) Comparison of ΔL_p of the measurements and simulations on the octave band 1000 Hz (global levels) plotted around the median of the measurements for the four configurations (A, B, C, D) and according to the three microphone distances (50, 100, and 200 m). Measurements are depicted by boxplots (without outliers), and simulations are depicted by linked dashes, with the same colors as in Fig. 11.

complex areas, the composition of the snowpack, the surface shape, and the presence of rocks may require more complex ground impedance modeling. If more complete and more complex propagation models are possible in the future, it is to the detriment of the computational cost, which is a parameter to be taken into account for parametric studies. The expected gain in terms of accuracy is also not guaranteed if one is not able to characterize the medium in more detail.

IV. VARIABILITY OF THE COMMUNICATION ACTIVE SPACE

The propagation model is now applied to investigate the influence of the topography, the meteorological conditions, and the source altitude on the AS of rock ptarmigans. Here, the source is considered static with a height above the ground defined as the typical flight altitude of the bird.

A. Description

The study is done for another site in the French Alps, which is chosen because a population of rock ptarmigans lives on this site all year round, especially during the breeding season (Canonne *et al.*, 2020; Marin-Cudraz *et al.*, 2019; Novoa *et al.*, 2019). This site is the Flaine ski resort (45.99 N, 6.73 E, 2400 m a.s.l.) and is referred to as "Flaine" in the remainder of this section. Its topography is presented in Fig. 13. DEM data of the bare ground with 5 m resolution were provided by the French National Geographic Institute (IGN: Institut national de l'information géographique et forestière). To avoid any sharp slopes, a low-pass filter has been applied to the topography. This smoothing procedure is reasonable since the actual snow layer naturally fills the depressions in the ground. The acoustic properties of the snow cover are identical in all configurations. They are chosen as $e = 0.15$ m, $R_s = 20\,000$ Pa · s · m^{-2}, $\Omega = 0.6$, $q^2 = 1.66$ to be representative of a moderately compacted snow as measured by Datt *et al.* (2016). The meteorological conditions are imposed using wind speed and temperature profiles from MOST (see Sec. III A 2) and a wind direction from south to north. The pressure field calculation is done within a 500 m radius around the point source. All the following maps are oriented with north at the top in the present section.

B. Results

1. Influence of topography

The ASs are computed for the four positions on the Flaine site presented in Fig. 13. These positions illustrate typical situations encountered in mountain environments: terrain with a steep slope (P1), gentle slope (P3), a promontory (P2), and a valley (P4). To isolate topographic effects, nearly homogeneous conditions are considered, with $u_* = 0.05$ m·s^{-1}, and $\theta_* = 0$.

Maps of the propagation loss are plotted in Fig. 14 for the four positions indicated in Fig. 13 on the Flaine site. They show that the shape of the AS depends significantly on the topography. Even in homogeneous atmospheric conditions, AS is therefore neither circular nor symmetrical over uneven landforms. In details, for P1, sound propagates preferentially toward the west, down the slope. For P2, the AS has a comparably small area and is essentially limited to the top of the promontory. For P3, the AS is discontinuous: it is made of a disk with a radius of about 200 m centered at the source and of small spots that can be seen at a large distance from the source (up to 500 m). Finally, for P4, the steep slopes of the valley prevent sound from propagating, and the AS is restricted to the bottom of the valley. In addition, the striations noticeable on P1 and P4 correspond to interference patterns due to the monochromatic calculation. Such pattern would not be visible in a broadband calculation.

2. Influence of meteorological conditions

The impact of meteorological conditions on the AS is now investigated. For that, the AS is calculated as a function

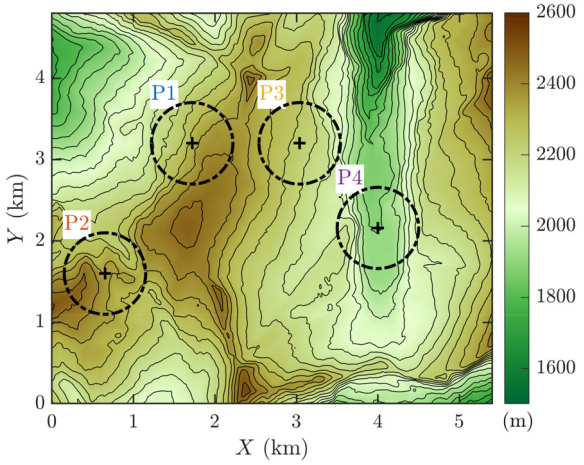

FIG. 13. (Color online) Topography of the Flaine ski resort, x, y positions of sources marked with crosses and circular computation domains for AS estimation (1, 2, 3, 4) in thick dotted lines. The map is oriented north up, and 50 m contour lines are drawn in thin black lines.

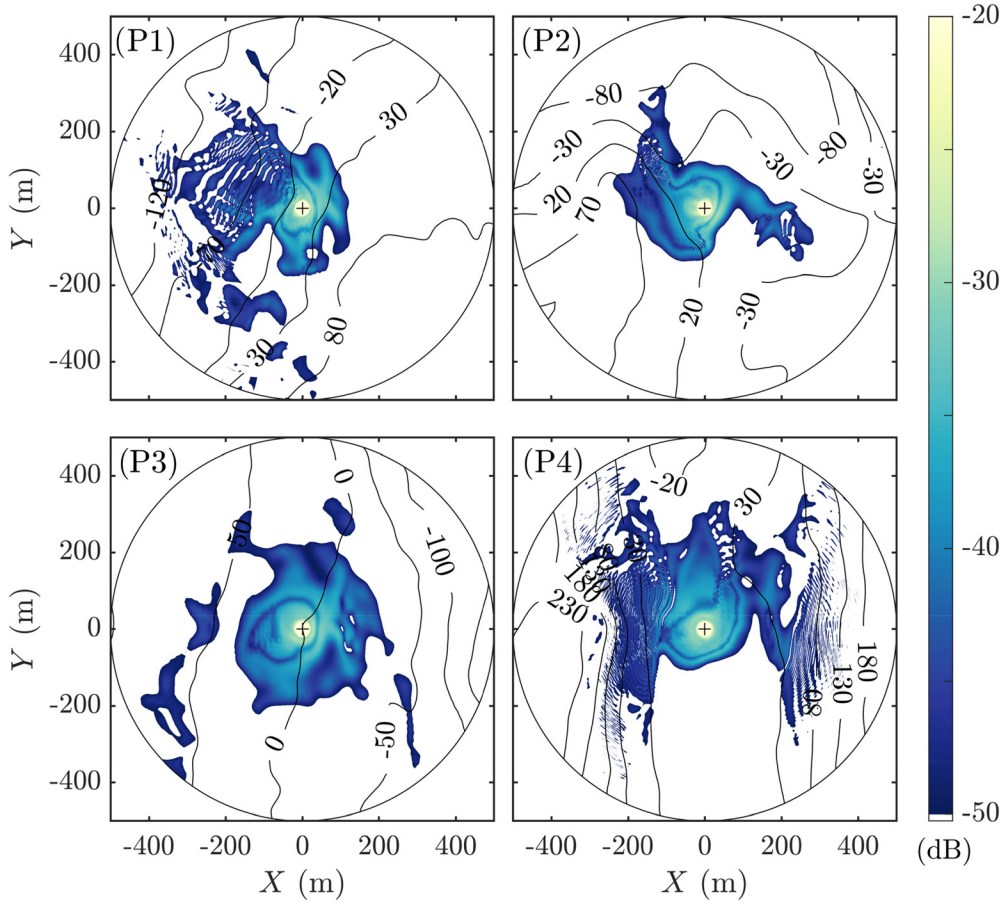

FIG. 14. (Color online) Map of the PL for the four positions (shown in Fig. 13) at 1 m height for a 1000 Hz frequency signal in nearly homogeneous atmospheric conditions: $u_* = 0.05\,\mathrm{m\cdot s^{-1}}$, $\theta^* = 0\,\mathrm{K}$, $z_S = 10\,\mathrm{m}$. Contour lines are drawn every 50 m in thin lines.

of the governing parameters for the wind and temperature profiles defined in Sec. III A 2. For the wind, the relevant parameter is still the friction velocity u_*. However, for the temperature, the sensible heat flux Q_H is now chosen instead of θ_*, because of its simpler physical interpretation. Indeed, the sensible heat flux represents the transfer of heat to the surface from the overlying air induced by the temperature difference between the ground surface and the atmosphere. It is related to u_* and θ_* by $Q_H = -\theta_* \rho_0 c_p u_*$, where c_p is the specific heat at constant pressure. The sensible heat flux depends on solar radiation and cloud cover. Thus, on a clear night, we have $Q_H < 0$, which leads to a positive temperature gradient and, hence, a positive sound speed gradient that favors sound propagation at long range. On the contrary, $Q_H > 0$ on a clear day, inducing a negative sound speed gradient that opposes sound propagation.

The AS is first computed for several values of the sensible heat flux Q_H and $u_* = 0.3\,\mathrm{m\cdot s^{-1}}$. Corresponding MOST parameters and weather conditions are given in Table IV. The values chosen for Q_H have been taken from Ostashev and Wilson (2016), and measurement data over snow were provided in Mott *et al.* (2013). They are assumed to be representative of the snow radiation behavior. Maps of PL for position 1 are shown in Fig. 15. Thus, a change from $Q_H = 400\ \mathrm{W\cdot m^{-2}}$, corresponding to a clear daytime [Fig. 15(c)], to $Q_H = -100\ \mathrm{W\cdot m^{-2}}$, corresponding to a clear nighttime over snow [Fig. 15(a)], induces an increase in the area of 30%.

Calculations of the AS are then performed for several values of u_* and for $Q_H = 0\ \mathrm{W\cdot m^{-2}}$. The chosen values of u_*, which are 0.05, 0.3, 0.7, and 1.1 m/s, induce wind speed values at 2 m height of $U_{(2m)} = 0.4$, 2.2, 5.2, and 8.2 m/s, respectively. These values imply a large scale of wind conditions, from very low to very strong wind, which slightly outstrips the proposed wind scale values of Ostashev and Wilson (2016). The corresponding maps of PL for position 1 are shown in Fig. 16. Increasing u_* tends to enlarge the shadow zone upwind and to reduce the AS accordingly.

TABLE IV. Conditions used in AS calculations, derived from the sensible heat flux: MOST parameters, wind speed 2 m above the ground, and celerity gradient in the wind direction $\Delta c^+_{\mathrm{eff}}$.

Condition	Q_H ($\mathrm{W\cdot m^{-2}}$)	u_* ($\mathrm{m\cdot s^{-1}}$)	θ_* (K)	L_{MO} (m)	$U_{(2m)}$ ($\mathrm{m\cdot s^{-1}}$)	$\Delta c^+_{\mathrm{eff}}$ ($\mathrm{m\cdot s^{-1}}$)
Clear daytime	400	0.3	−1.38	−4.6	1.7	−2.1
Daytime	200	0.3	−0.69	−9	1.9	−0.2
Mostly cloudy	0	0.3	0	$-\infty$	2.2	3.8
Nighttime	−50	0.3	0.17	36.6	2.4	7.8
Clear nighttime	−100	0.3	0.36	18.3	2.6	13.1

https://doi.org/10.1121/10.0011545

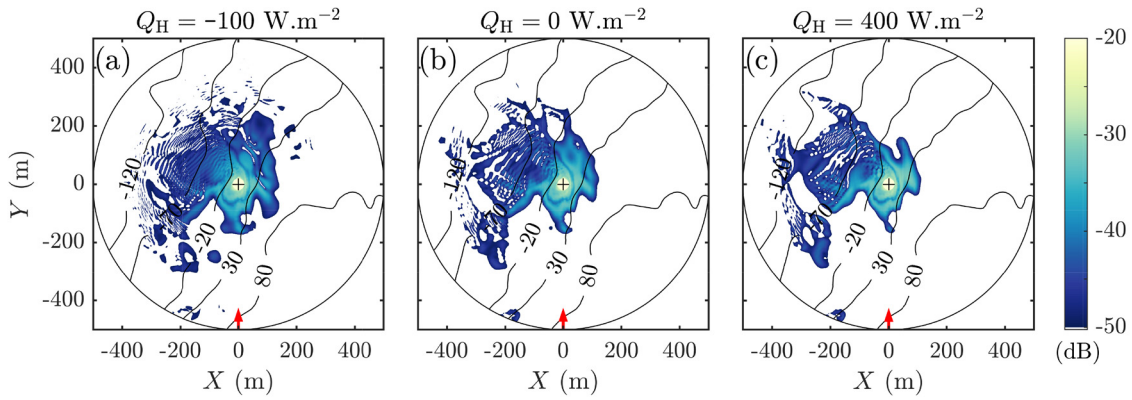

FIG. 15. (Color online) Map of the PL for different values of Q_H, at 1 m height, for a 1000 Hz frequency signal, and at P1 (shown in Fig. 13). Reference case is (b), with values $u_* = 0.3\,\mathrm{m \cdot s^{-1}}$, $Q_H = 0\,\mathrm{W \cdot m^{-2}}$, $z_S = 10$ m. Plots (a) and (c), respectively, depict the influence of sensible heat flux from $Q_H = -100$ to $400\,\mathrm{W \cdot m^{-2}}$. All other parameters are the same as the reference case. Contour lines are drawn every 50 m in thin lines. The red arrow depicts u_* and the wind direction.

In addition, a modest increase in the AS area is noticed downwind in the northeast direction for $u_* = 1.1\,\mathrm{m{\cdot}s^{-1}}$ [Fig. 16(c)]. Overall, the AS area is reduced by 33% when increasing u_* from 0.05 to $1.1\,\mathrm{m{\cdot}s^{-1}}$.

As previously shown for the plains habitat, nighttime provides a favorable condition for atmospheric propagation because of the temperature inversion (Larom *et al.*, 1997). The shape of the AS is also modified by wind speed and direction but still limited by the underlying landform.

3. Influence of source height

Finally, the influence of the source height on the AS is estimated. Calculations are performed for $Q_H = 0\ \mathrm{W{\cdot}m^{-2}}$, $u_* = 0.3\ \mathrm{m{\cdot}s^{-1}}$, and z_S between 1 and 50 m. The PL maps are plotted in Fig. 17 for position 1. The source height has a considerable influence on the AS area. When the source moves up from $z_S = 1$ m [Fig. 17(a)], the area increases by 102% for $z_S = 10$ m [Fig. 17(b)] and by +282% for $z_S = 50$ m [Fig. 17(c)]. Besides, the AS tends to be more circular as z_S increases, until it becomes a disk for a sufficiently high source, as seen for $z_S = 50$ m [Fig. 17(c)].

The results obtained here are consistent with previous studies. In forest environments, Dabelsteen *et al.* (1993), Holland *et al.* (1998), and Mathevon *et al.* (2005) showed that small changes in roost height may result in a significant increase in AS. In addition, Mathevon *et al.* (1996) highlight the importance of the singing post to limit song degradation during propagation. The crucial role of the singing height in the AS was also noticed in open areas by Jensen *et al.* (2008) in hooded crow: individuals improve their signaling condition when in flight or perched compared to the ground feeding situation. Here, the increase in the AS with source height is generalized to an uneven landform.

4. Influence of environmental parameters on different topography

Next, the influence of environmental parameters on the AS area are discussed for the four positions on the Flaine site. For comparison purposes, the area ratio (%) is introduced as A/A_{ff}, where A_{ff} is the AS area obtained in free field for the same attenuation threshold. In free field, one has $\mathrm{PL} = -20\log_{10}(R)$, and the parameter A_{ff} can then be simply calculated with $A_{ff} = \pi R_{ff}^2$, where R_{ff} is the

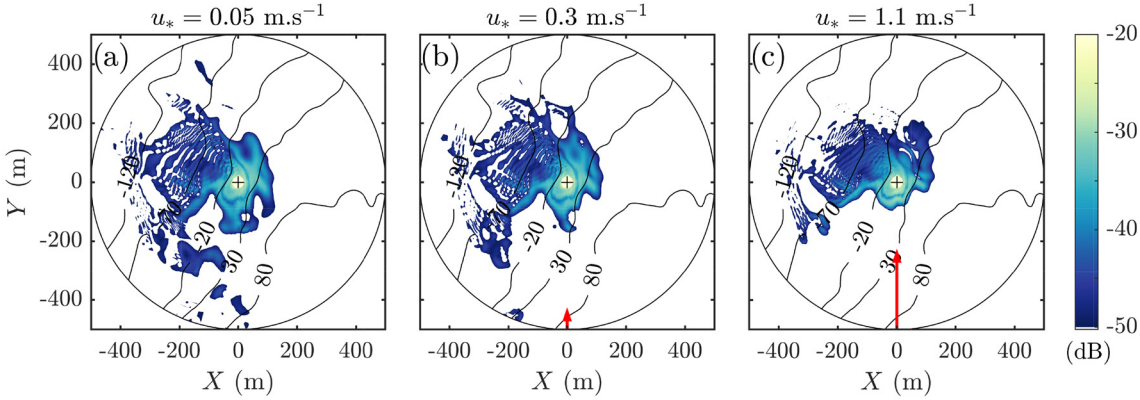

FIG. 16. (Color online) Map of the PL for different values of u_*, at 1 m height, for a 1000 Hz frequency signal, and at P1 (shown in Fig. 13). Reference case is (b), with $u_* = 0.3\,\mathrm{m \cdot s^{-1}}$, $Q_H = 0\,\mathrm{W \cdot m^{-2}}$, $z_S = 10$ m. Plots (a) and (c), respectively, depict the wind influence between $u_* = 0.05$ and $1.1\,\mathrm{m \cdot s^{-1}}$. All other parameters are the same as the reference case. Contour lines are drawn every 50 m in thin lines. The red arrow depicts u_* and the wind direction.

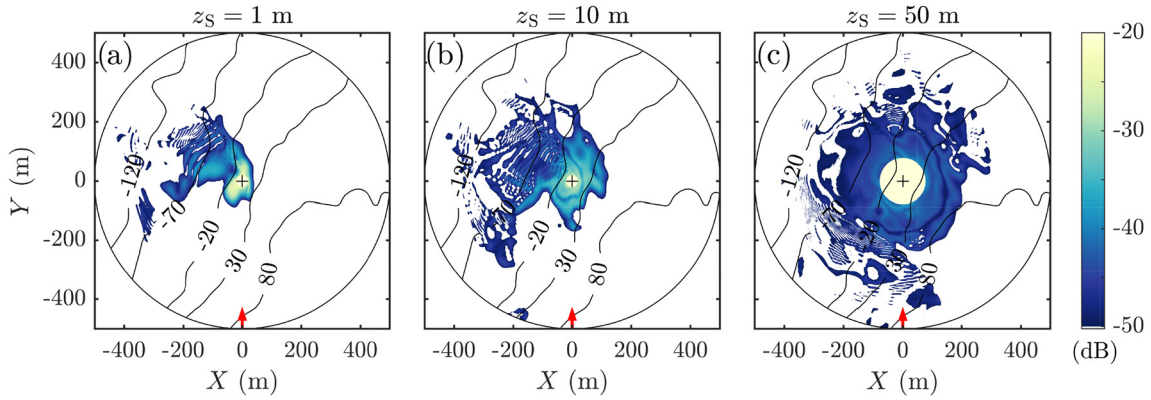

FIG. 17. (Color online) Map of the PL for different values of z_S, at 1 m height, for a 1000 Hz frequency signal, and at P1 (shown in Fig. 13). Reference case is (b), with values of $u_* = 0.3\,\mathrm{m \cdot s^{-1}}$, $Q_H = 0\,\mathrm{W \cdot m^{-2}}$, $z_S = 10$ m. Plots (a) and (c), respectively, show the influence of the source height above ground from $z_S = 1$ to 50 m. All other parameters are the same as the reference case. Contour lines are drawn every 50 m in thin lines. The red arrow depicts u_* and the wind direction.

maximum distance of detection in free field, which is equal to $R_{ff} = 10^{50/20} \approx 316$ m for a threshold of –50 dB.

Figure 18 shows the variation of the area ratio as a function of u_*, Q_H, and z_S for the four positions. The increase in the friction velocity from $u_* = 0.05$ to $1.1\,\mathrm{m \cdot s^{-1}}$ induces for all positions a reduction of the area, which varies between –4% and –23% depending on the topography. A similar reduction of the area in a range between –11% and –38% is estimated for the first three positions with the increase in Q_H from –100 to $400\,\mathrm{W \cdot m^{-2}}$. A slight augmentation of 7% is, however, noticed for position 4. This is due to its location in a valley: upward refraction leads to increased SPLs higher up in the valley. Regarding the source height, its increase from 1 to 50 m implies in all cases a large increase in the AS area, by +37% for position 4 in a valley and up to +75% for position 3 on a gentle slope.

In conclusion, the AS is dependent on the topography, the wind and temperature profiles, and the source position. Both area and shape of the AS are changed by the modification of one of these conditions. We have shed light on two predominant factors: first the topography, which constrains the spatial limits of the AS whatever the atmospheric conditions are, and second the source height. Particularly, it can be deduced that performing a display flight while singing allows the rock ptarmigan to augment its AS but also to overcome the constraint of the topographic heterogeneity.

V. CONCLUSION

The variability of the AS was investigated for the rock ptarmigan in mountain environment using numerical simulations. A model for atmospheric sound propagation based on the PE was proposed to calculate the AS. It accounts for the topography, the ground impedance, the wind and temperature profiles, and the atmospheric absorption. An experimental campaign was carried out in the French Alps to evaluate the model against long-range sound propagation measurements. Despite some uncertainties regarding weather conditions and snow impedance, a good agreement was obtained between calculations and measurements.

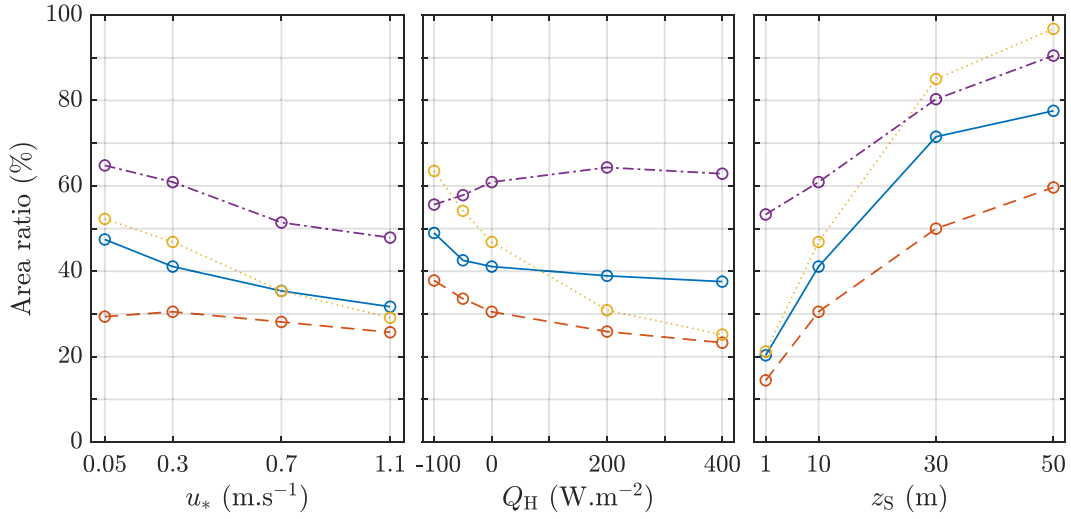

FIG. 18. (Color online) Variations of the area ratio with the friction velocity u_*, the sensible heat flux Q_H, and the source height z_S for the four positions shown in Fig. 13: 1 (blue solid), 2 (orange dashed), 3 (yellow dotted), 4 (violet dashed-dotted).

The variability was also correctly reproduced by the propagation model under most conditions.

The propagation model was then applied to calculate the AS. The influence of the topography, the meteorological conditions, and the source altitude on the AS was examined. It was shown that the AS is clearly asymmetric. Therefore, considering an effective distance is not relevant for such a heterogeneous environment since the AS shape is mostly driven by the underlying topography. Moreover, the source height was shown to be also a decisive parameter impacting the size and the shape of the AS. Especially, it was concluded that the display flight allows the rock ptarmigan to increase its AS and to overcome the landform heterogeneity encountered in mountain ranges. AS also depends to a lesser extent on weather conditions. The AS variability can be expected both in space, according to the movements of the birds on their territories, and in time, from day to day and even from hour to hour.

The propagation model proposed in the paper can be used to estimate AS in various habitat and weather conditions. It can be used to study communication networks and their spatial and temporal dynamics. In addition, the ability to deduce temporal signal after its propagation is likely to provide interesting clues concerning the degradation of information carried by the vocalization (Mouterde *et al.*, 2014). However, it should be noted that the generalization and application of such a model to other species will require the knowledge of several parameters: SL, hearing threshold, and background noise. An appropriate estimation of acoustic communication networks could provide insights into species behaviors, like territory defense and mating strategy. It also opens up new possibilities for automated counting techniques using audio recorders.

ACKNOWLEDGMENTS

This research is supported by the Labex CeLyA of Université de Lyon (ANR-10-LABX-0060). A collaboration with the Centre d'Etudes de la Neige (UMR 3589), Grenoble, France, allowed us to conduct experiments on a maintained instrumented alpine site. Isabelle Gouttevin made this collaboration possible. Yannick Deliot provided meteorological data and helped with site logistics at Col du Lac Blanc. Hugo Merzisen provided the topographic data at Col du Lac Blanc. Hervé Bellot provided additional meteorological data. Léo Papet took part in the propagation experiments and impedance measurements. Simulations were made possible by access to the high-performance computing resources of PMCS2I (Pôle de Modélisation et de Calcul en Sciences de l'Ingénieur et de l'Information) of Ecole Centrale de Lyon. We would like to thank Codor Khodr and Michael Greenfield for their helpful comments on the manuscript.

Albert, D. G. (**2001**). "Acoustic waveform inversion with application to seasonal snow covers," J. Acoust. Soc. Am. **109**(1), 91–101.

ANSI/ASA (**2010**). S1.18, *Method for Determining the Acoustic Impedance of Ground Surfaces, Accredited Standards Committee S1, Acoustics*, American National Standard (revision of ANSI S1.18-1999) (Acoustical Society of America, New York).

Attenborough, K., and van Renterghem, T. (**2021**). *Predicting Outdoor Sound*, 2nd ed. (CRC, Boca Raton, FL).

Aubin, T., and Mathevon, N. (**2020**). *Coding Strategies in Vertebrate Acoustic Communication* (Springer, Cham, Switzerland).

Bérengier, M. C., Stinson, M. R., Daigle, G. A., and Hamet, J. F. (**1997**). "Porous road pavements: Acoustical characterization and propagation effects," J. Acoust. Soc. Am. **101**(1), 155–162.

Blairon, N., Blanc-Benon, P., Bérengier, M., and Juvé, D. (**2002**). "Outdoor sound propagation in complex environment: Experimental validation of a PE approach," in *Proceedings of the 10th International Symposium on Long Range Sound Propagation*, September 12–13, Grenoble, France, pp. 114–128.

Bossert, A. (**1977**). "Bestandesaufnahmen am Alpenschneehuhn (*Lagopus mutus*) im Aletchgebiet" ["Inventory of the rock ptarmigan population (Lagopus mutus) in the Aletsch region (Swiss Alps)]," Der Ornithologische Beobachter **74**, 95–98.

Brenowitz, E. A. (**1982**). "The active space of red-winged blackbird song," J. Comp. Physiol. **147**(4), 511–522.

Canonne, C., Novoa, C., Muffat-Joly, B., Resseguier, J., Desmet, J.-F., Casadesus, J. B., Arvin-Berod, M., and Besnard, A. (**2020**). "Life on the edge: Common slow pace of life but contrasted trajectories of alpine rock ptarmigan populations at their southern margin," Wildl. Biol. **2020**(2), 1–11.

Collino, F. (**1997**). "Perfectly matched absorbing layers for the paraxial equations," J. Comput. Phys. **131**(1), 164–180.

Dabelsteen, T., Larsen, O. N., and Pedersen, S. B. (**1993**). "Habitat-induced degradation of sound signals: Quantifying the effects of communication sounds and bird location on blur ratio, excess attenuation, and signal-to-noise ratio in blackbird song," J. Acoust. Soc. Am. **93**(4), 2206–2220.

Dabelsteen, T., and Mathevon, N. (**2002**). "Why do songbirds sing intensively at dawn? A test of the acoustic transmission hypothesis," Acta Ethologica **4**(2), 65–72.

Darden, S. K., Pedersen, S. B., Larsen, O. N., and Dabelsteen, T. (**2008**). "Sound transmission at ground level in a short-grass prairie habitat and its implications for long-range communication in the swift fox *Vulpes velox*," J. Acoust. Soc. Am. **124**(2), 758–766.

Datt, P., Kapil, J. C., Kumar, A., and Srivastava, P. K. (**2016**). "Experimental measurements of acoustical properties of snow and inverse characterization of its geometrical parameters," Appl. Acoust. **101**, 15–23.

Dooling, R. J., and Leek, M. R. (**2018**). "Communication masking by man-made noise," in *Effects of Anthropogenic Noise on Animals*, edited by H. Slabbekoorn, R. J. Dooling, A. N. Popper, and R. R. Fay (Springer, New York), pp. 23–46.

Dragna, D., Blanc-Benon, P., and Poisson, F. (**2014**). "Impulse propagation over a complex site: A comparison of experimental results and numerical predictions," J. Acoust. Soc. Am. **135**(3), 1096–1105.

Embleton, T. F. W. (**1996**). "Tutorial on sound propagation outdoors," J. Acoust. Soc. Am. **100**(1), 31–48.

Forrest, T. G. (**1994**). "From sender to receiver: Propagation and environmental effects on acoustic signals," Am. Zool. **34**(6), 644–654.

Guillaume, G., Faure, O., Gauvreau, B., Junker, F., Bérengier, M., and L'Hermite, P. (**2015**). "Estimation of impedance model input parameters from *in situ* measurements," Appl. Acoust. **95**, 27–36.

Guyomarc'h, G., Bellot, H., Vionnet, V., Naaim-Bouvet, F., Déliot, Y., Fontaine, F., Puglièse, P., Nishimura, K., Durand, Y., and Naaim, M. (**2019**). "A meteorological and blowing snow data set (2000–2016) from a high-elevation alpine site (Col du Lac Blanc, France, 2720 m a.s.l.)," Earth Syst. Sci. Data **11**(1), 57–69.

Henwood, K., and Fabrick, A. (**1979**). "A quantitative analysis of the dawn chorus: Temporal selection for communicatory optimization," Am. Naturalist **114**(2), 260–274.

Holland, J., Dabelsteen, T., Pedersen, S. B., and Larsen, O. N. (**1998**). "Degradation of wren *Troglodytes troglodytes* song: Implications for information transfer and ranging," J. Acoust. Soc. Am. **103**(4), 2154–2166.

ISO (**1993**). ISO 9613-1:1993(E), "Acoustics—Attenuation of sound during propagation outdoors—Part 1: Calculation of the absorption of sound by the atmosphere," (International Organization for Standardization, Geneva, Switzerland).

Jensen, K. K., Larsen, O. N., and Attenborough, K. (**2008**). "Measurements and predictions of hooded crow (*Corvus corone cornix*) call propagation over open field habitats," J. Acoust. Soc. Am. **123**(1), 507–518.
Johnsgard, P. A. (**2008**). "14 Rock ptarmigan," in *Grouse and Quails of North America* (University of Nebraska, Lincoln, NE), pp. 225–239.
Khodr, C., Azarpeyvand, M., and Green, D. N. (**2020**). "An iterative three-dimensional parabolic equation solver for propagation above irregular boundaries," J. Acoust. Soc. Am. **148**(2), 1089–1100.
Larom, D., Garstang, M., Payne, K., Raspet, R., and Lindeque, M. (**1997**). "The influence of surface atmospheric conditions on the range and area reached by animal vocalizations," J. Exp. Biol. **200**(3), 421–431.
Lengagne, T., and Slater, P. J. B. (**2002**). "The effects of rain on acoustic communication: Tawny owls have good reason for calling less in wet weather," Proc. R. Soc. Lond. B **269**(1505), 2121–2125.
Li, K. M., Waters-Fuller, T., and Attenborough, K. (**1998**). "Sound propagation from a point source over extended-reaction ground," J. Acoust. Soc. Am. **104**(2), 679–685.
Lihoreau, B., Gauvreau, B., Bérengier, M., Blanc-Benon, P., and Calmet, I. (**2006**). "Outdoor sound propagation modeling in realistic environments: Application of coupled parabolic and atmospheric models," J. Acoust. Soc. Am. **120**(1), 110–119.
Lohr, B., Wright, T. F., and Dooling, R. J. (**2003**). "Detection and discrimination of natural calls in masking noise by birds: Estimating the active space of a signal," Anim. Behav. **65**(4), 763–777.
Loning, H., Griffith, S. C., and Naguib, M. (**2022**). "Zebra finch song is a very short-range signal in the wild: Evidence from an integrated approach," Behav. Ecol. **33**(1), 37–46.
MacDonald, S. (**1970**). "The breeding behavior of the rock ptarmigan," Living Bird **9**, 195–238.
Marin-Cudraz, T., Muffat-Joly, B., Novoa, C., Aubry, P., Desmet, J.-F., Mahamoud-Issa, M., Nicolè, F., Van Niekerk, M. H., Mathevon, N., and Sèbe, F. (**2019**). "Acoustic monitoring of rock ptarmigan: A multi-year comparison with point-count protocol," Ecol. Indic. **101**, 710–719.
Marten, K., and Marler, P. (**1977**). "Sound transmission and its significance for animal vocalization," Behav. Ecol. Sociobiol. **2**, 271–290.
Mathevon, N., Aubin, T., and Dabelsteen, T. (**1996**). "Song degradation during propagation: Importance of song post for the wren *Troglodytes troglodytes*," Ethology **102**(3), 397–412.
Mathevon, N., Aubin, T., Vielliard, J., da Silva, M.-L., Sebe, F., and Boscolo, D. (**2008**). "Singing in the rain forest: How a tropical bird song transfers information," PLoS ONE **3**(2), e1580.
Mathevon, N., Dabelsteen, T., and Blumenrath, S. H. (**2005**). "Are high perches in the blackcap *Sylvia atricapilla* song or listening posts? A sound transmission study," J. Acoust. Soc. Am. **117**(1), 442–449.
McGregor, P. K. (**2005**). *Animal Communication Networks* (Cambridge University, Cambridge, MA).
McGregor, P. K., and Dabelsteen, T. (**1996**). "Communication networks," in *Ecology and Evolution of Acoustic Communication in Birds*, edited by D. E. Kroodsma and E. H. Miller (Cornell University, Ithaca, NY), pp. 409–425.
Monin, A. S., and Obukhov, A. M. (**1954**). "Basic laws of turbulent mixing in the surface layer of the atmosphere," Contrib. Geophys. Inst. Acad. Sci. USSR **151**, 163–187.
Moore, H. M., Attenborough, K., Rogers, J., and Lee, S. (**1991**). "*In-situ* acoustical investigations of deep snow," Appl. Acoust. **33**, 281–301.
Mott, R., Gromke, C., Grünewald, T., and Lehning, M. (**2013**). "Relative importance of advective heat transport and boundary layer decoupling in the melt dynamics of a patchy snow cover," Adv. Water Resources **55**, 88–97.
Mouterde, S. C., Theunissen, F. E., Elie, J. E., Vignal, C., and Mathevon, N. (**2014**). "Acoustic communication and sound degradation: How do the individual signatures of male and female zebra finch calls transmit over distance?," PLoS ONE **9**(7), e102842.
Nordtest (**1999**). "Ground surfaces: Determination of the acoustic impedance," NT ACOU 104, Project 1365-97 (Nordtest, Taastrup, Denmark).
Novoa, C., Desmet, J.-F., Brenot, J.-F., Muffat-Joly, B., Arvin-Bérod, M., Resseguier, J., and Tran, B. (**2019**). "Demographic traits of two alpine populations of rock ptarmigan," in *Ecology, Conservation, and Management of Grouse*, edited by B. K. Sandercock, K. Martin, and G. Segelbacher (University of California, Oakland, CA), pp. 267–280.
Ostashev, V. E., Juvé, D., and Blanc-Benon, P. (**1997**). "Derivation of a wide-angle parabolic equation for sound waves in inhomogeneous moving media," Acta Acust. united Acust. **83**, 455–460.
Ostashev, V. E., and Wilson, D. K. (**2016**). *Acoustics in Moving Inhomogeneous Media* (CRC, London).
Ostashev, V. E., Wilson, D. K., and Muhlestein, M. B. (**2020**). "Wave and extra-wide-angle parabolic equations for sound propagation in a moving atmosphere," J. Acoust. Soc. Am. **147**(6), 3969–3984.
Parris, K. M. (**2002**). "More bang for your buck: The effect of caller position, habitat and chorus noise on the efficiency of calling in the spring peeper," Ecol. Modell. **156**(2), 213–224.
Raynor, E. J., Whalen, C. E., Bomberger Brown, M., and Powell, L. A. (**2017**). "Location matters: Evaluating Greater Prairie-Chicken (*Tympanuchus cupido*) boom chorus propagation," Avian Conserv. Ecol. **12**(2), art 17.
Reichert, M. S., Enriquez, M. S., and Carlson, N. V. (**2021**). "New dimensions for animal communication networks: Space and time," Integr. Comp. Biol. **61**(3), 814–824.
Reiners, W. A., and Driese, K. L. (**2001**). "The propagation of ecological influences through heterogeneous environmental space," BioScience **51**(11), 939–950.
Ręk, P., and Osiejuk, T. S. (**2011**). "Nonpasserine bird produces soft calls and pays retaliation cost," Behav. Ecol. **22**(3), 657–662.
Salomons, E. M. (**2001**). *Computational Atmospheric Acoustics* (Springer, Dordrecht, Netherlands).
Watson, A. (**1972**). "The behaviour of ptarmigan," Br. Birds **65**(1), 6–26.
Wiley, R. H., and Richards, D. G. (**1978**). "Physical constraints on acoustic communication in the atmosphere: Implications for the evolution of animal vocalizations," Behav. Ecol. Sociobiol. **3**(1), 69–94.
Wilson, D. K. (**1993**). "Relaxation-matched modeling of propagation through porous media, including fractal pore structure," J. Acoust. Soc. Am. **94**(2), 1136–1145.